



## Review

## Evolution of interfacial voids in Cu-to-Cu joints

Hung-Che Liu<sup>a,b</sup>, Shih-Chi Yang<sup>a,b</sup>, Jia-Juen Ong<sup>a,b</sup>, Dinh-Phuc Tran<sup>a,b</sup>, A.M. Gusak<sup>c</sup>, K.N. Tu<sup>d,e</sup>, Chih Chen<sup>a,b,\*</sup>

<sup>a</sup> Department of Materials Science and Engineering, National Chiao Tung University, Hsinchu 30010, Taiwan

<sup>b</sup> Department of Materials Science and Engineering, National Yang Ming Chiao Tung University, Hsinchu 30010, Taiwan

<sup>c</sup> Department of Physics, Cherkasy National University, Ukraine

<sup>d</sup> Department of Materials Science and Engineering, City University of Hong Kong, Hong Kong

<sup>e</sup> Department of Electrical Engineering, City University of Hong Kong, Hong Kong



## ARTICLE INFO

## Keywords:

Cu-to-Cu bonding technology

Interfacial voids

Void ripening

Interfacial elimination

## ABSTRACT

In this study, the Cu joints were fabricated by Cu pads with the highly (111)-oriented nano-twinned structure at 250 °C. We reported a new characterization approach by plan-view images of focused ion beam (FIB) to observe the evolution of interfacial voids in the Cu joints under annealing. The distribution function of interfacial voids and the kinetics of void evolution were then studied and analyzed. The evolution of interfacial voids was proposed to occur at different stages, which were dominant by plastic deformation, creep deformation, and void ripening caused by grain boundary and lattice diffusion. Significant void ripening was observed at early stage of bonding attributed to fast grain boundary diffusion. However, after the bonding interface was eliminated, the void sizes did not change due to slow lattice diffusion.

## 1. Introduction

To enhance the performance of electronic chips, heterogeneous integration was considered a good candidate. Three-dimensional integrated circuit (3D IC) interconnection has been the most important packaging technology in the next generation. The general interconnection joints used in 3D IC are solder joints in the past decade [1]. To increase the input/output number, the bump size and the pitch needed to be shrunk. However, the solder joints were observed to have side wetting and bridge failure when the solder joints were shrunk [2,3]. Cu/SiO<sub>2</sub> hybrid bonding technology was a good choice to resolve these problems [4]. The Cu joints replaced the solder joints and the dielectric layer replaced the underfill process. In 2016, hybrid bonding was used in CMOS images sensor [5] and the bump pitch was shrunk to about 10 μm. In recent years, there were many researches which achieved sub-10 μm and sub-micron pitch [6–8].

Because hybrid bonding technology would bond the Cu interconnection joints and the dielectric layer under solid state, the hybrid bonding could achieve ultra-fine pitch. Cu-to-Cu joints were fabricated in many methods. One of them was surface activated bonding (SAB) [9,10]. It can achieve the Cu joints at room temperature, but the ultra-high vacuum atmosphere was needed to avoid the activated surface

being oxidized. The process would be very expensive. The general method of metal bonding was thermocompression bonding [11–18]. Cu joints would be under pressure at high temperature and the diffusion would happen to obtain reliable interconnection. The bonding pressure, temperature, and time are correlated with roughness [19] and surface orientation [15,16]. The Cu surface would be easily oxidized at high temperature. Some researchers would cap a passivation layer to avoid the surface oxidation [20–24]. Above researchers observed the Cu joints through many instruments to make sure they obtained reliable joints. The interfacial voids were difficult to be totally eliminated.

In this study, the evolution of interfacial voids would be observed by plan-view images of bonding interfaces. The void size distribution was obtained by software. The variation of average void size under different bonding conditions could be obtained. Then, the kinetic model of Cu joints fabrication was proposed by the evolution of interfacial voids.

## 2. Experimental

In this study, first the highly (111)-oriented nano-twinned Cu pads were electroplated on the 8-in. patterned silicon wafers. A direct current (DC) of 8 ASD (A/dm<sup>2</sup>) was used to grow the Cu pads. The electroplating bath contains 0.8 M CuSO<sub>4</sub>, 40 ppm Cl<sup>-</sup>, 100 g/L H<sub>2</sub>SO<sub>4</sub>, and the nt-Cu

\* Corresponding author at: Department of Materials Science and Engineering, National Chiao Tung University, Hsinchu 30010, Taiwan.

E-mail address: [chihchen@nycu.edu.tw](mailto:chihchen@nycu.edu.tw) (C. Chen).

<https://doi.org/10.1016/j.matchar.2022.112085>

Received 18 April 2022; Received in revised form 3 June 2022; Accepted 20 June 2022

Available online 28 June 2022

1044-5803/© 2022 Elsevier Inc. All rights reserved.

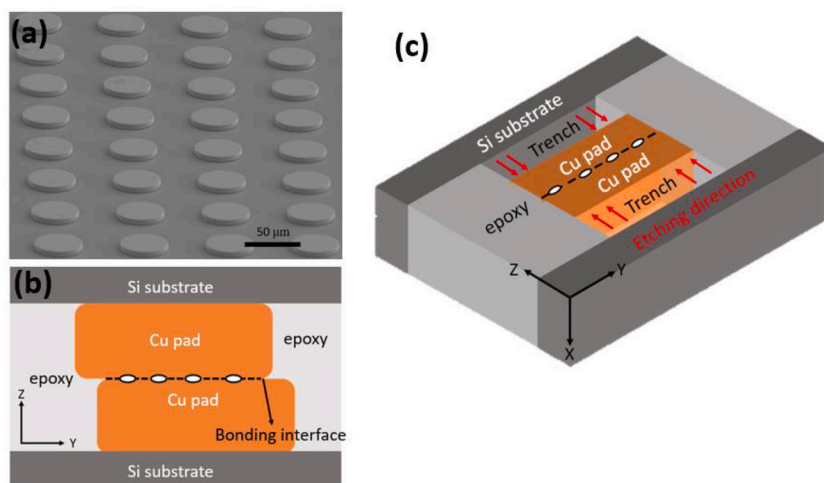


**Fig. 1.** Schematic diagram of fabricating TEM lamella used to observe plan-view images at bonding interface. (a) The fabricated Cu pads array. (b) Schematic diagram of the Cu joints cross-sectional images, and (c) TEM lamella fabrication of the Cu joints during FIB etching.

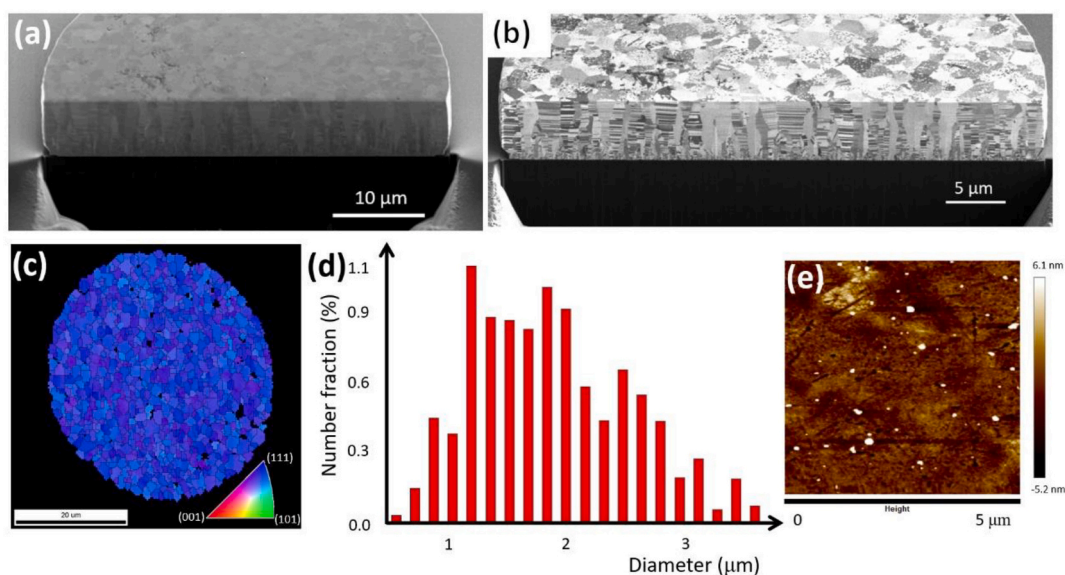


**Fig. 2.** Schematic diagrams showing the preparation of the plan-view TEM lamella. (a) Cross-sectional electron beam image of the Cu pads after FIB etching. (b) Cross-sectional ion beam image of the Cu pads after FIB etching. (c) Plan-view orientation image maps of the Cu pads and the inverse pole figure. (d) Grain size distribution of the Cu pads and (d) results of AFM scanning.

additive, which was provided by Chemleader INC. After the electroplating process, chemical mechanical planarization (CMP) was performed to flatten the Cu surface, and the Cu pads which were 45  $\mu\text{m}$  in diameter and 7  $\mu\text{m}$  in height were obtained, as shown in Fig. 1(a). After the CMP process, to obtain the suitable size of the top and the bottom dies, a dicing process was executed. The top die size was 6  $\times$  6  $\text{mm}^2$  and bottom die size was 15  $\times$  15  $\text{mm}^2$ . The surface orientation was analyzed by electron backscattered diffraction (EBSD) and the surface roughness was measured by atomic force microscope (AFM).

A bonding machine with an alignment function was employed to bond the top and the bottom dies. Before bonding, a simple cleaning process was performed to clean the Cu surface of both dies. First, the dies

were immersed by acetone and vibrated in an ultrasound machine to remove organic pollutants. Then, the dies were rinsed by isopropyl and deionized water. Second, the dilute hydrochloric acid was employed to clean the oxide on the surface. The bonding holders were used to fasten both dies and were put into the bonding machine in vacuum. The vacuum level was 4 Pa. The bonding temperature was set to 250  $^{\circ}\text{C}$ , and the downforce was 300 N. The average ramp-up and ramp-down rates were  $\sim$  10 and 1  $^{\circ}\text{C}/\text{s}$ , respectively. To study the evolution of interfacial voids under different annealed conditions, the annealed time was 5, 15, 30, and 120 min.

After the bonding process, to observe the voids at bonding interface, focused ion beam (FIB) and transmission electron microscope (TEM)

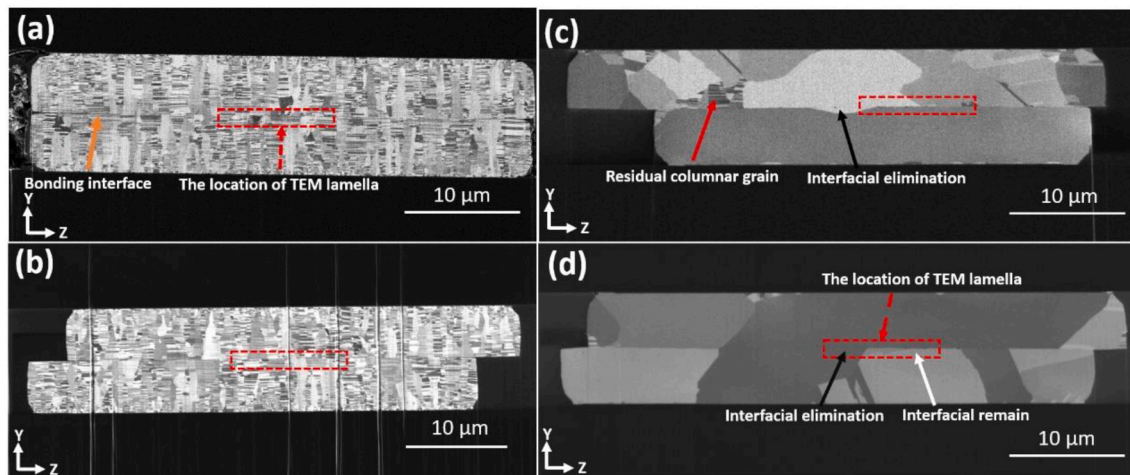


**Fig. 3.** Cross-sectional ion beam images of the Cu-Cu joint bonded at 250 °C for different annealed duration. The joints were annealed for (a) 5 min, (b) 15 min, (c) 30 min and (d) 120 min. The red dotted rectangles were the location of TEM lamellas for interfacial void observation. (For interpretation of the references to color in this figure legend, the reader is referred to the web version of this article.)

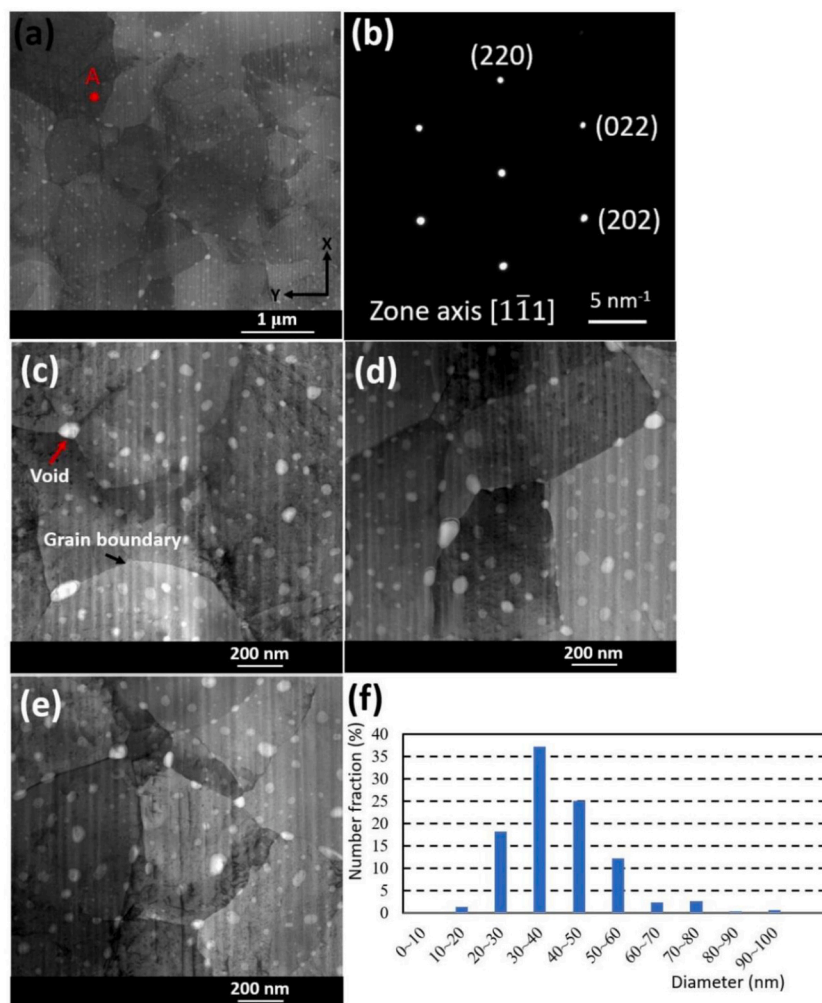


**Fig. 4.** Plan-view images were captured under the bright field mode TEM. The Cu-Cu joint was bonded at 250 °C for 5 min. (a) Low magnification image presenting the joint and (b) selected area diffraction pattern at point A. (c)-(e) High magnification plan-view images of bonding interface showing the interfacial voids. (f) Void size distribution of 296 voids in (c) to (e).

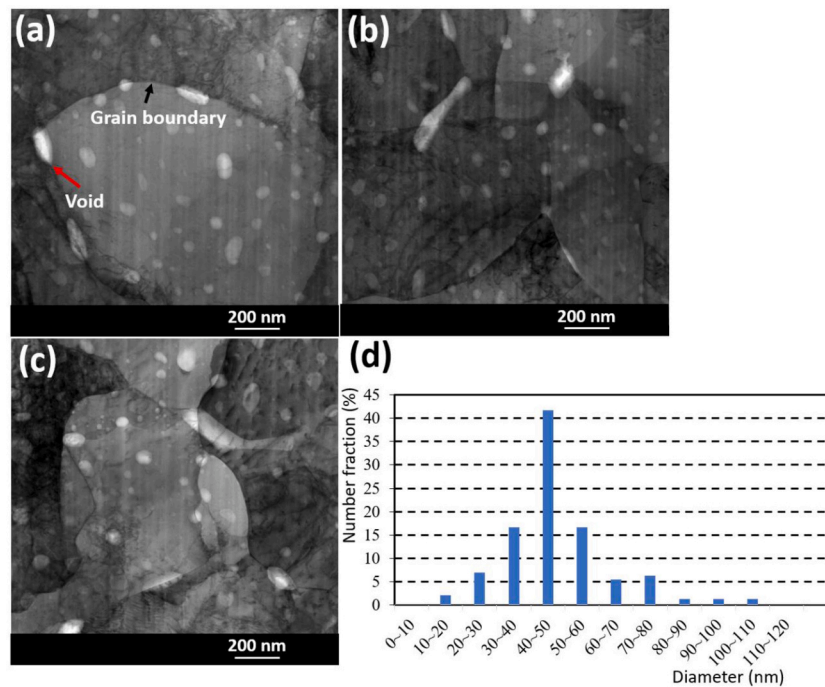


**Fig. 5.** Plan-view images were captured under the bright field mode TEM. The Cu-Cu joint was bonded at 250 °C for 15 min. (a)-(c) High magnification plan-view images of bonding interface showing the interfacial voids. (d) Void size distribution of 144 voids in (a) to (c).

were employed. To avoid damaging the Cu during a grinding process, epoxy was used to fill up the gaps between two joints. The embedded samples were ground to the position of the Cu joints by a grinding machine. FIB was employed to etch the surface which was vertical to the bonding interface. The schematic diagram of Cu joints after FIB etching is shown in Fig. 1(b). The electron images of FIB were used to confirm whether the bonding result of Cu joints is successful or not. The ion images of FIB can observe the microstructure of the Cu joints. Although the cross-sectional images can observe the interfacial voids in high magnification, the density of interfacial voids was too little to calculate the voids size with this analysis.

Plan-view images of bonding interfaces are good at observing the interfacial voids. The schematic diagram of plan-view method is shown in Fig. 1(c). First, the bonded sample was put on the FIB holder and noted that the bonding interface was vertical to the plane of the FIB holder. Then, ion beams along the direction of the horizontal interface were used to etch two sides of the bonding interface, shown as red arrows in Fig. 1(c). If the electron images with voids appeared on two sides, the ion beam should stop etching. Thus, the TEM lamella of the plan-view interface could be achieved.

### 3. Results and discussion

The images of post-CMP Cu pads were shown in Fig. 2. Fig. 2(a) and (b) show the electron and ion images from FIB, respectively. In Fig. 2(b), the columnar grain with layer twins can be observed. Fig. 2(c) shows the plan-view orientation image maps of the Cu pads. The inverse pole figure (IPF) is shown in the right corner of Fig. 2(c). The blue color indicated (111) orientation. The images show that the bonding surface was highly preferred (111) orientation. The (111) ratio was higher than

95% and the grain size was about  $1.43 \pm 0.54 \mu\text{m}$  in diameter. The grain size distribution is presented in Fig. 2(d). The result of AFM is shown in Fig. 2(e). The scanning area was  $5 \times 5 \mu\text{m}^2$ . The root mean squared roughness was about 1.8 nm.

The images of Cu joints microstructure are shown in Fig. 3. The annealed time was 5, 15, 30 and 120 min in Fig. 3(a) to (d), respectively. The red dotted rectangle in each figure was the location of TEM lamella to be cut. In Fig. 3(a) and (b), the columnar grain with layer twins still existed. However, in Fig. 3(c), the columnar grain was eliminated by grain growth. The red arrow indicated the residual columnar grain. The black arrow indicated that the bonding interface was eliminated by grain growth. In Fig. 3(d), the eliminated bonding interface, which is denoted as “interfacial elimination” in this paper, was observed, but part of the bonding interface was existing, which is denoted as “interfacial remain”. To understand the variation of the voids across or not across the interface, we choose the location of TEM lamella at the conjunction of crossing and not crossing the interface.

In a short summary, as the annealed time increased at 250 °C, the columnar grain started to be eliminated between 15 and 30 min. Then, the bonding interface would have an opportunity to be eliminated by grain growth. The evolution of interface voids will be observed in the next part.

Figs. 4 to 7 show the TEM images of the plan-view interface which are located in the red dotted rectangles in Fig. 3(a) to (d), respectively. First, the sample which has been annealed for 5 min at 250 °C is shown in Fig. 4. Fig. 4(a) presents the plan-view image of the bonding interface under low magnification. It can be observed that there were some grains which were similar to the plan-view EBSD images of the Cu pads with some tiny white dots. The white dots could be the location of the interfacial voids. Because the TEM images were captured under bright

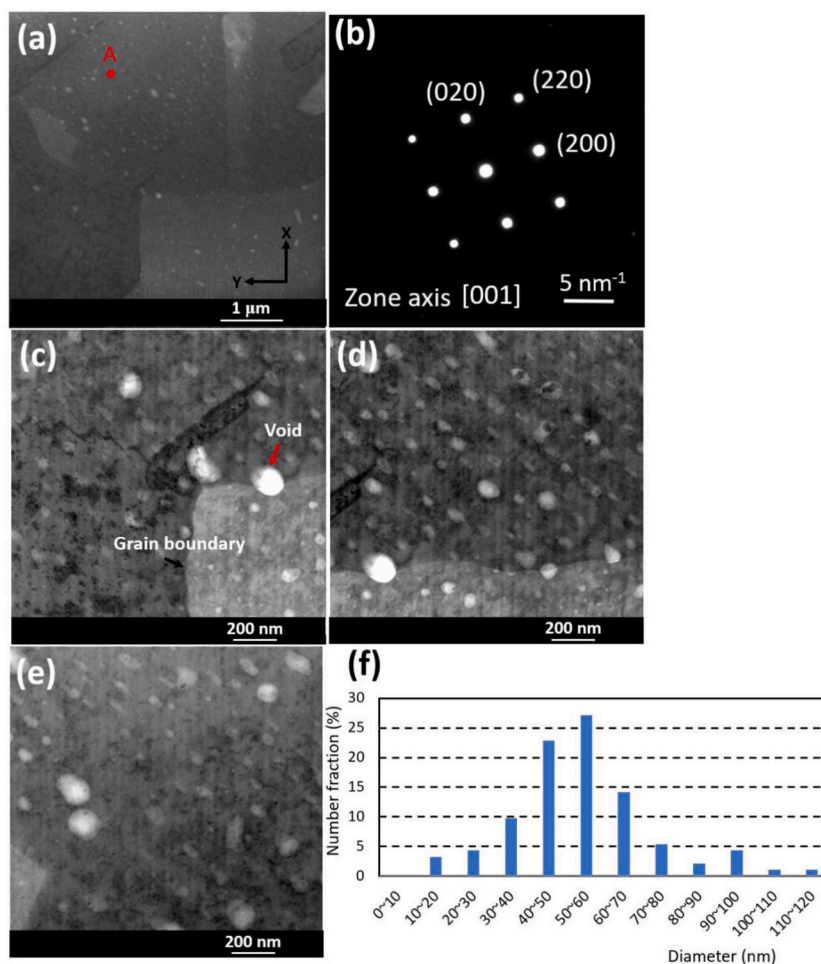


**Fig. 6.** Plan-view images were captured under the bright field mode TEM. The Cu-Cu joint bonded at 250 °C for 30 min. (a) Low magnification image presenting the joint and (b) selected area diffraction pattern at point A. (c)-(e) High magnification plan-view images of bonding interface showing the interfacial voids. (f) Void size distribution of 92 voids in (c) to (e).

field mode, different thickness would cause different contrasts. The voids area was a thinner thickness than the no-voids area, so voids area would be the white area in bright field images. The selected area diffraction (SAD) at point A is shown in Fig. 4(b). The diffraction pattern was hexagonal so its zone axis was  $\langle 111 \rangle$  direction. The SAD result confirmed that the bonding interface was the same as the surface of the as-deposited Cu pads. To measure the size of voids, the high magnification images are shown in Fig. 4(c) to (e). The voids size was  $40 \pm 12$  nm in diameter, and the total void number was 296 in these three images. The voids size distribution is shown in Fig. 4(f). It seems that the size distribution was close to a normal distribution. The voids size peaked between 30 nm and 40 nm. Fig. 5 shows the results of the sample annealed for 15 min at 250 °C. Because the low magnification images were similar to those of samples annealed for 5 min, we only showed the high magnification images and the voids size distribution in Fig. 5. The voids size was  $48 \pm 16$  nm in diameter and the total voids number was 144 in these three images. The voids size distribution is shown in Fig. 5 (d). The voids size peaked between 40 nm and 50 nm. Fig. 6 shows the results of samples annealed for 30 min at 250 °C. The low magnification

image is presented in Fig. 6(a). We can observe that the grains have obviously grown and had some voids. We used SAD to obtain the diffraction pattern, as shown in Fig. 6(b), and we found that the zone axis was  $\langle 001 \rangle$  direction.

The orientation has transformed from  $\langle 111 \rangle$  surface to  $\langle 200 \rangle$  surface after the sample was annealed for 30 min at 250 °C. The transformation is due to reduction of the total energy after annealing process; the surface energy and strain energy would compete with each other [25,26]. It is known that the  $\langle 200 \rangle$  orientation has lower strain energy than the  $\langle 111 \rangle$  orientation. The  $\langle 200 \rangle$ -oriented grains nucleated at the transition layer and grew with the annealing time. They completely transformed to the  $\langle 200 \rangle$ -oriented grains in order to lower the total energy. The high magnification images are presented in Fig. 6(c) to (e). The void size distribution is shown in Fig. 6(f). The average void size in diameter was  $57 \pm 24$  nm. The total void count in these three images was 92. The void size peaked between 50 nm and 60 nm.

The results of sample annealed for 120 min at 250 °C are presented in Fig. 7. In Fig. 7(a), a unique phenomenon was observed. The left grain had more and larger voids than that of the right grain. Fig. 7(b) and (c)

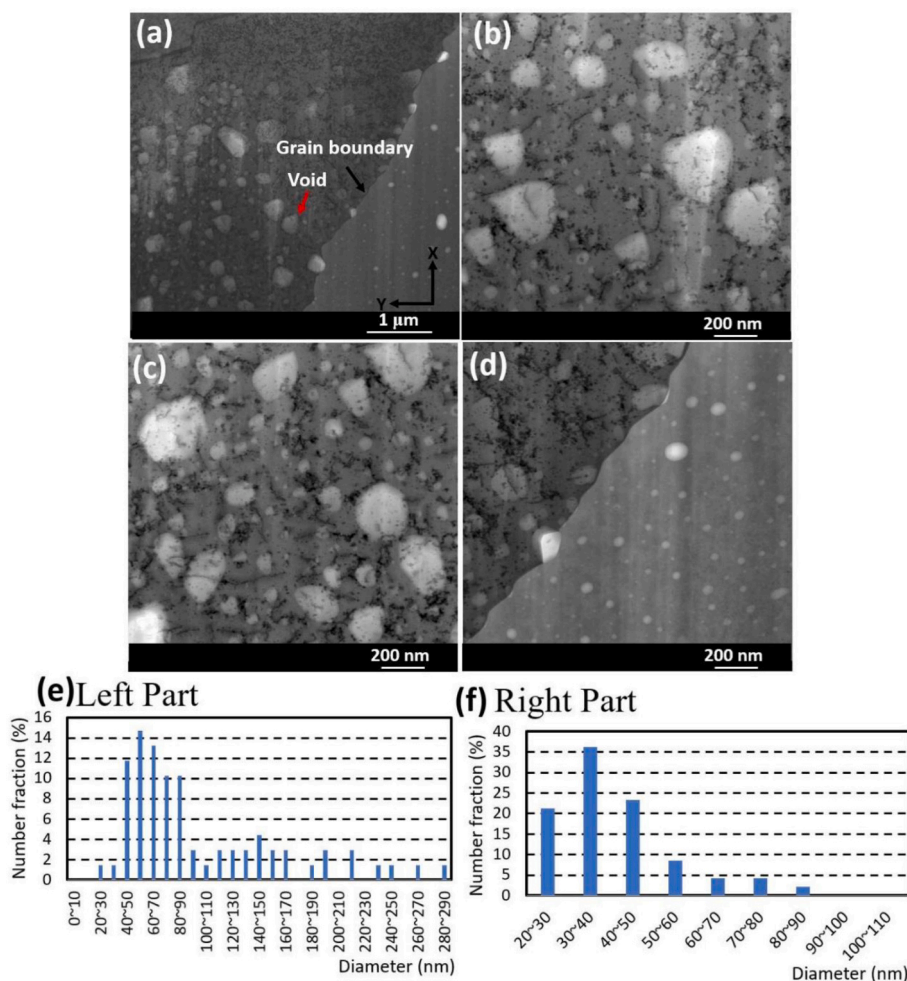


**Fig. 7.** Plan-view images were captured under the bright field mode TEM. The Cu-Cu joint bonded at 250 °C for 120 min. (a) Low magnification image presenting the joint. (b)-(c) High magnification images at the left grain, (d) High magnification images at the right grain. (e) Void size distribution of 68 voids in left grain. (f) Void size distribution of 47 voids in left grain.

are high magnification images from the left grain. Fig. 7(d) is the high magnification image from the right grain. The void size distributions of left grain and right grain are shown in Fig. 7(e) and (f), respectively. For the voids located in the left grain, the average void size in diameter was  $100 \pm 60$  nm. The void count in these images was 68. >30% voids were larger than 100 nm in diameter. However, for the voids which located in the right grain, the average void size in diameter was  $41 \pm 14$  nm. The void count was 47. The void size peaked between 30 and 40 nm. From cross-sectional images which are shown in Fig. 3(d), we speculated that the interfacial elimination and interfacial remain would affect the evolution of interfacial voids. According to Ref. [27], if the interface remains, the interfacial voids will grow with the annealing time, and this phenomenon was based on the void ripening effect.

The void ripening effect was also observed in this study, based on the results of annealed for 5, 15 and 30 min, where the average void size became larger as the annealed time increased. As shown in Fig. 3(a) to (c), the interface remains were observed. Some regions in Fig. 3(d) possessed the interfacial remains, and another one was with the interfacial eliminated. Because the interfacial voids in the left grain in

Fig. 7(a) would continue to grow to 100 nm, it seems that the left grain would be the region where the interface remains. The right grain would be the region where the interface has been eliminated. This is because the diffusion pathway would change from grain boundary diffusion to lattice diffusion. Therefore, it seems that the growth or ripening of the interfacial voids would stop when grain growth has occurred across the interface.

To clarify why our Cu joints can have both interface elimination and interface remain, the energy-dispersive X-ray spectroscopy (EDX) in STEM was used to analyze the element distribution in samples after annealing for 120 min at 250 °C. The results are presented in Fig. 8, where Fig. 8(a) shows the low magnification bright field image in TEM mode and the red square is the analyzed area. Fig. 8(b) presents the dark field image in STEM mode. The black part was the location of voids in this mode and the dotted line was the grain boundary. Fig. 8(c) to (e) are the EDX element mapping analysis of Cu, O and C, respectively. Fig. 9 presents the EDX line scanning analysis. Fig. 9(a) is the analyzed area. Fig. 9(b) and (c) are the line scanning analysis of Cu and O, respectively. From the above results, the signal of Cu would drop down at the location

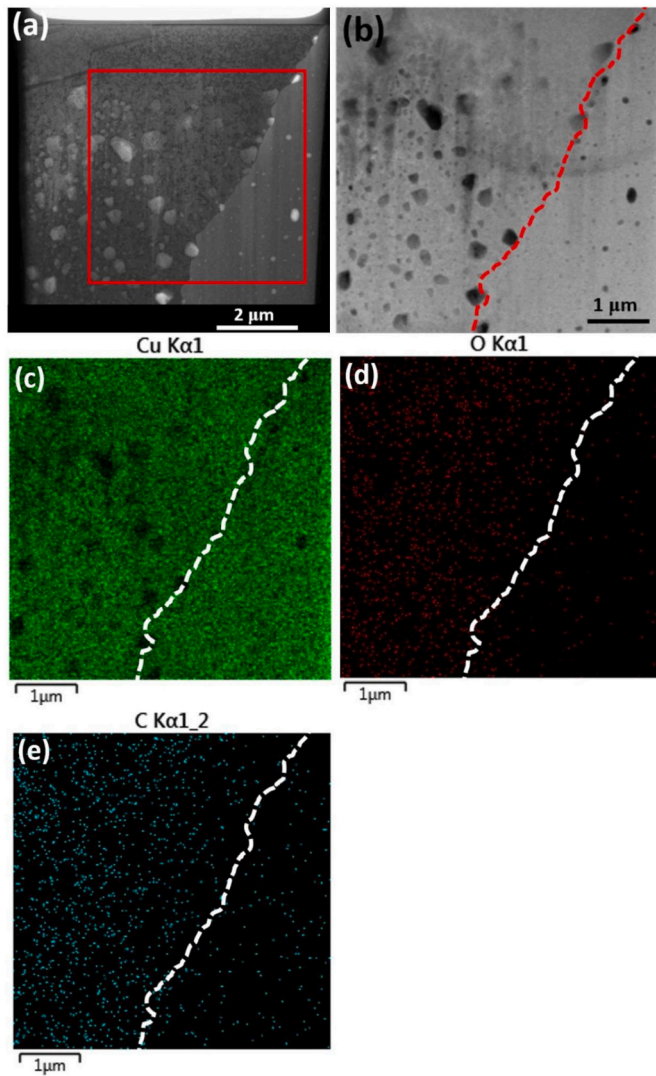


**Fig. 8.** EDX element mapping analysis in the Cu-Cu joints bonded at 250 °C for 120 min. (a) Bright field mode image of the TEM lamella and (b) dark field mode image in STEM. (c) Cu signal map. (d) O signal map. (e) C signal map. The dotted line was the location of the grain boundary.

of voids. However, more signals of O and C were found in the left grain. Therefore, the left grain contained more impurities than the right grain. Because the impurity would block the grain boundary movement in the left grain [28], the interfacial grain boundary could remain and the interfacial voids would continue to grow.

To confirm that the interfacial voids would freeze in grains which have interface elimination, the Cu-to-Cu bonded samples were employed to fabricate larger-area-interfacial-elimination Cu joints. The blanked Si substrate with 100 nm Ti as adhesion layer and 200 nm Cu as seed layer was used to fabricate nt-Cu films. The electrodeposition and planarization were the same as reported before. The bonding process was two steps in this case. The first step was 250 °C for 30 min and the bonding pressure was 24 MPa. To achieve a larger area of interfacial elimination, the second step was 300 °C for 120 min under 1 MPa. The cross-sectional images after the bonding process are presented in Fig. 10 (a) and (b), and the interfacial elimination can be confirmed.

To observe the interfacial voids in the sample, two trenches were etched by FIB. First trench was etched after the bonding process. The other one was etched after the bonding process and annealing for 180 min at 300 °C. The schematic image and the plan-view image after FIB etching are presented in Fig. 10(c) and (d), respectively. When the ion beam etching was close to the bonding interface, we slowed down the etching rate and captured many images during the etching process. We stopped the etching process until the interfacial voids disappeared. Then, images were overlapped together to obtain the void size. Fig. 11 is the results of the analysis method, where Fig. 11(a) and (b) are plan-view images of samples without and with annealing for 180 min at 300 °C, respectively. They are the SEM images which are the closest to the bonding interface.

Fig. 11(c) and (d) are the void size distributions of samples without and with annealing for 180 min at 300 °C, respectively. For the sample without the annealing, the average void size in diameter was  $75.7 \pm 30.9$  nm, and the total void count was 133. For the sample with the annealing process, the average void size in diameter was  $76.0 \pm 31.5$  nm, and the total void count was 140. These results confirmed that the interfacial voids were frozen when the interfacial elimination happened.

To model the voids freezing after the interfacial elimination, we assume that the interfacial voids would be buried in a grain, so the diffusion path was lattice diffusion in the contact zone and the surface creep driven by stress gradient was ignorable. Then, assuming that an isolated void of radius ( $R$ ) is situated in Cu with equilibrium concentration of vacancies around it, but the void is being dissolved by vacancy flux into the surrounding matrix because of Gibbs-Thomson capillary effect. The schematic diagram is presented in Fig. 12, and we estimate the time of void shrinkage below.

The Laplace pressure from curvature ( $R$ ) can be represented as  $2\gamma\Omega/R$  where  $\gamma$  is surface energy,  $\Omega$  is the atomic or vacancy volume and  $R$  is the radius of curvature. According to Gibbs-Thomson relation for the curvature, the vacancy concentration is represented as

$$X_v^{eq}(R) = X_v^{eq} + \frac{2\gamma\Omega}{kTR} X_v^{eq} \quad (1)$$

where  $X_v^{eq}$  is the equilibrium vacancy concentration,  $k$  is Boltzmann constant and  $T$  is the absolute temperature.

After taking the usual steady state approximation of bulk diffusion around a spherical void, and the Gibbs-Thomson relation for the curvature dependence of boundary concentration, we obtain the following flux balance equation at the moving boundary of the void:

$$\frac{4\pi R^2 dR}{dt} = 4\pi R^2 \cdot D_v \frac{X_v^{eq} - (X_v^{eq} + \frac{2\gamma\Omega}{kTR} X_v^{eq})}{R} = -4\pi R^2 D_v X_v^{eq} \frac{2\gamma\Omega}{kTR^2} \quad (2)$$

Consider that the product of vacancy diffusivity and the equilibrium fraction of vacant sites is approximately equal to self-diffusivity,  $D_v X_v^{eq} = D_{bulk}^*$  (if one neglects correlation factor), we obtain:

$$R^2 dR = -D_{bulk}^* \frac{2\gamma\Omega}{kT} dt \rightarrow R_0^3 - R^3(t) = 3 \cdot D_{bulk}^* \frac{2\gamma\Omega}{kT} t \quad (3)$$

Thus, the time of shrinking from some initial radius  $R_0$  to zero is equal to

$$t_{collapse} = \frac{R_0^3 - 0}{6D_{bulk}^* \gamma\Omega} kT \quad (4)$$

In Eq. (4), we take the initial radius to be 30 nm and the temperature to be 300 °C, the value of  $D_{bulk}^*(573 \text{ K}) \approx 4.87 \times 10^{-23} \text{ m}^2/\text{s}$ ,  $\gamma \approx 1 \text{ J/m}^2$ ,  $\Omega \approx 1 \times 10^{-29} \text{ m}^3$ , and  $k \approx 1.38 \times 10^{-23} \text{ J/K}$  [29,30], we obtain:

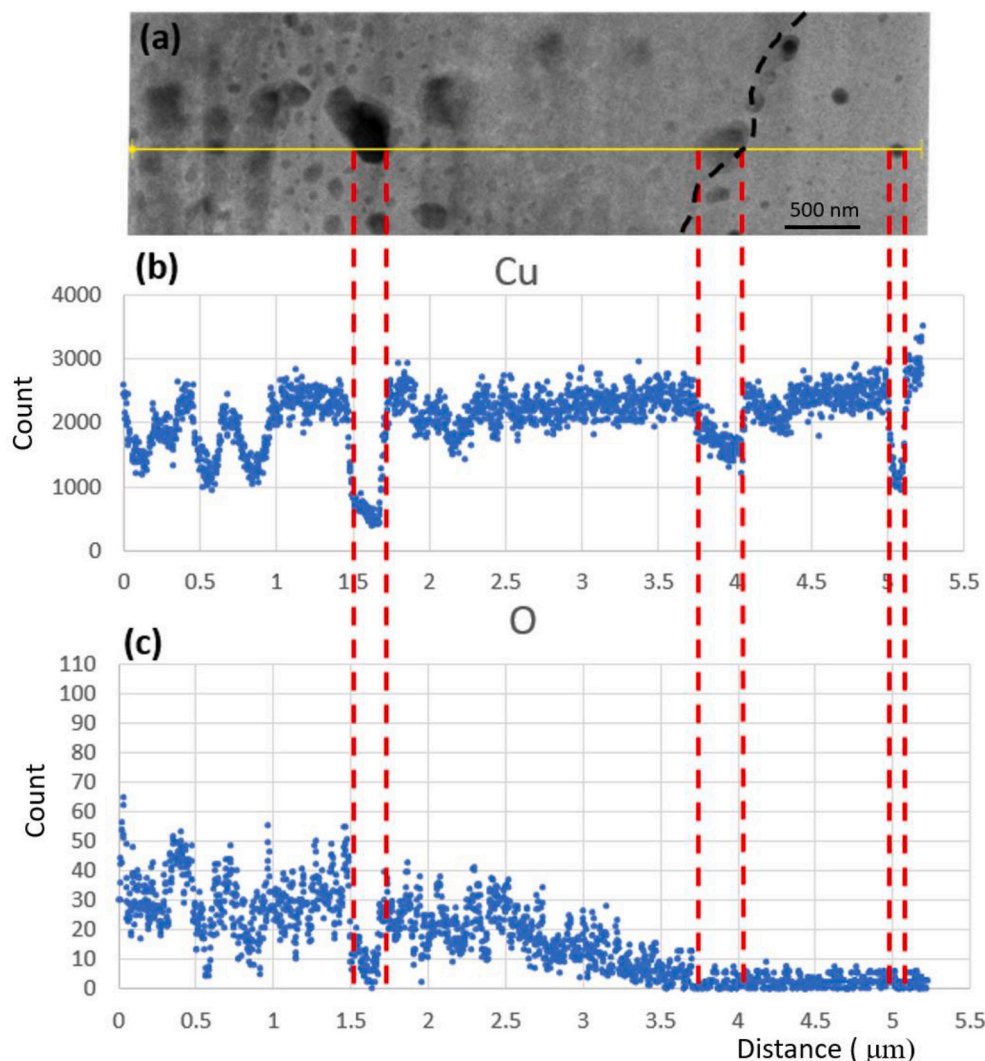


Fig. 9. EDX element line scanning analysis in the Cu-Cu joints bonded at 250 °C for 120 min. (a) Dark field mode image in STEM. (b) Cu signal map. (c) O signal map. The black dotted line was the location of the grain boundary.

$$\begin{aligned}
 t_{collapse}(R_0 = 30 \text{ nm}, T = 573 \text{ K}) \\
 &= \frac{(3 \times 10^{-8})^3}{6 \times 4.87 \times 10^{-23} \times 1 \times 10^{-29}} \times 1.38 \times 10^{-23} \times 573 \\
 &\approx 7.34 \times 10^7 \text{ s} \approx 20000 \text{ h}
 \end{aligned}$$

If the annealing time was 3 h, the 30-nm voids would maintain the same size from Eq. (4). Therefore, the void would shrink with a very slow rate. The interfacial voids with interfacial elimination would freeze in this study.

Finally, we try to unify the evolution of interfacial voids in Cu joints and the schematic images are presented in Fig. 13. Fig. 13(a) shows the two Cu surfaces which begin to contact each other. Because the contact area was very small, pressure applied on the contact area would be larger than the yield strength ( $\sigma_y$ ) of Cu. Plastic deformation would happen to make more contact areas until the pressure was lower than the yield strength. The duration of plastic deformation would be very short.

Fig. 13(b) presents the schematic images of Cu joints after plastic deformation has happened. The contact area would be a transition state between surface and grain boundary, and we called it to be the interfacial quasi-boundary. The diffusion coefficient in the quasi-boundary would be between that of surface and grain boundary. Under this state, the pressure was less than yield strength.

There is a stress gradient between the contact area and void area. Because of the stress gradient, high diffusion coefficient and the temperature, surface creep would happen. The Cu atom would diffuse from contact area to void area to shrink the interfacial voids and the contact area would become grain boundary. Creep model could explain the void shrinkage in the early stage [12,15,16,18].

Fig. 13(c) presents the schematic images of Cu joints at the end of creep deformation. In this stage, the stress gradient and diffusion coefficient were not enough to shrink the interfacial voids. The bonding interface would become an interfacial grain boundary and had a

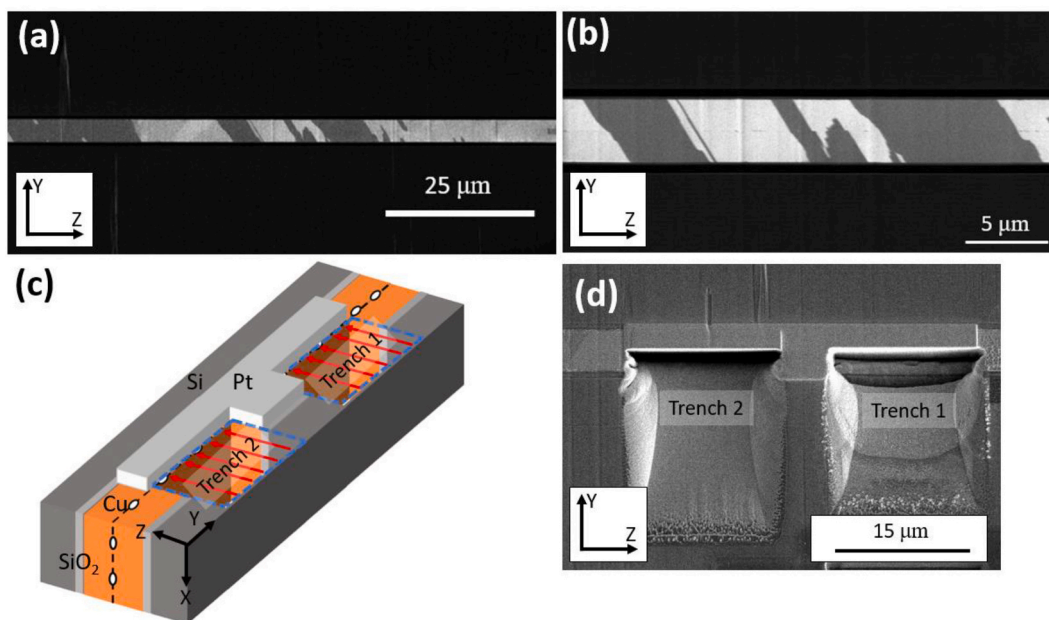


Fig. 10. Interfacial void observation in the same sample. (a)-(b) Cross-sectional ion beam images of Cu joints after the bonding process. (c) The schematic diagram of interfacial void observation in the same sample. (d) Top view image of Cu joints after void observation. Trench 1 observed the void without the post annealing process. Trench 2 observed the void with the post annealing process.

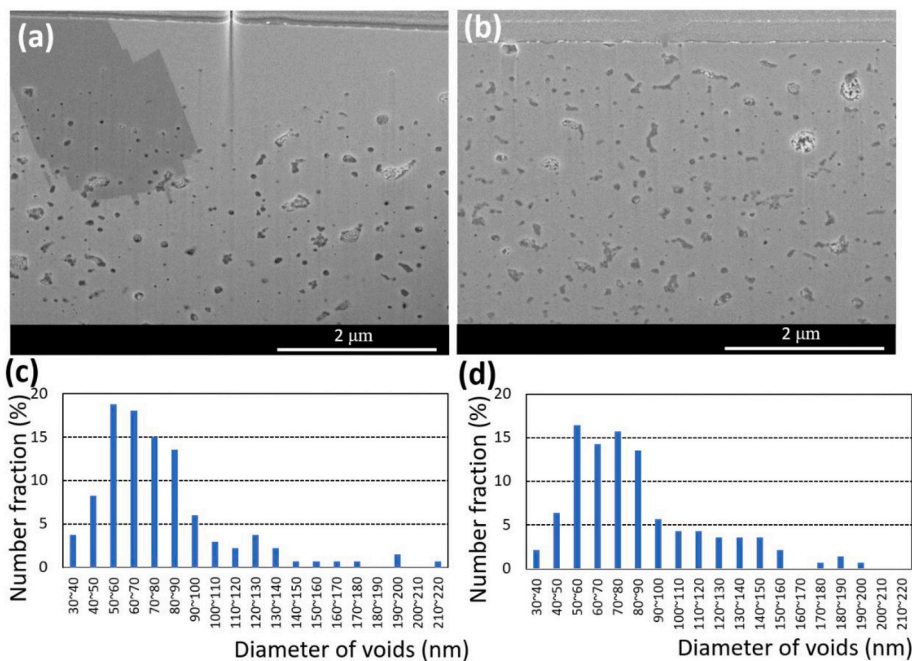


Fig. 11. Plan-view images at the bonding interface. (a) Void observation for Cu joints without 180-min at 300 °C post-annealing process. (b) Void observation for Cu joints with post-annealing process. (c) Void size distribution of 133 in (a). (d) Void size distribution of 140 in (b).

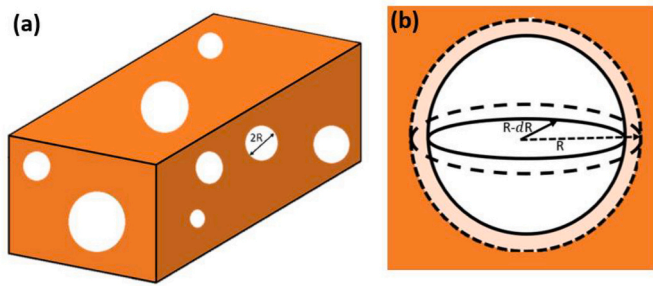


Fig. 12. Schematic diagram for modeling of the void shrinkage in lattice. (a) Imaging diagram of voids near the bonding interface. (b) Schematic image for void shrinkage.

with the higher annealed temperature at 300 °C for 180 min. We proposed that the diffusion path has changed from grain boundary to lattice after interface elimination has happened. Consequently, the void ripening stopped due to slow diffusion.

#### Data availability

The raw/processed data required to reproduce these findings cannot be shared at this time as the data also forms part of an ongoing study.

#### Declaration of Competing Interest

The authors declare no conflict of interest.

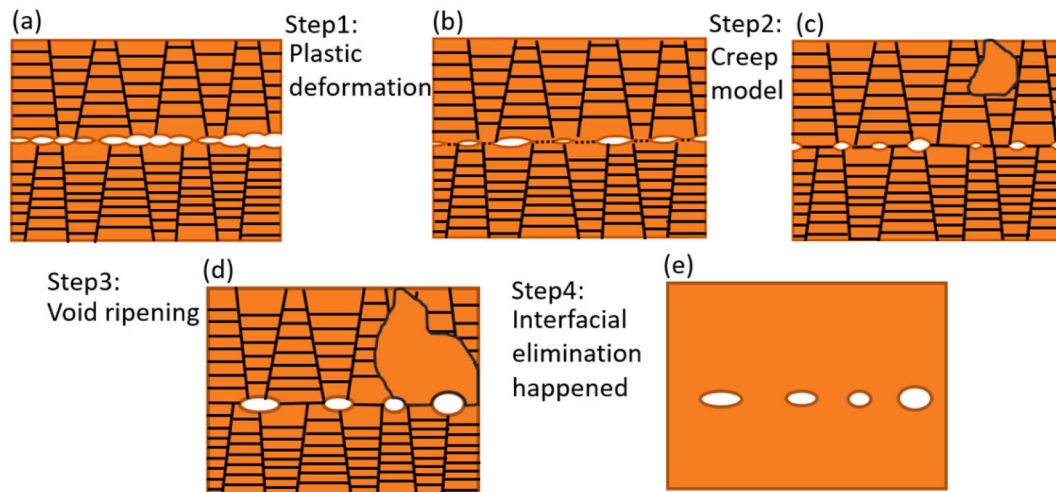


Fig. 13. Schematic diagram for the evolution of interfacial voids in each stage. (a) Schematic diagram for two Cu surfaces which begin to contact each other. (b) Schematic diagram for Cu joints after plastic deformation and the contact area would be interfacial semi-boundary. (c) Schematic diagram for Cu joints after creep deformation and the contact area would be interfacial grain boundary. (d) Schematic diagram for Cu joints in which the void ripening and the abnormal grain growth happened. (e) Schematic diagram for Cu joints which interfacial elimination happened.

distribution of interfacial voids. To lower the interfacial energy, the void ripening effect would cause aggregation of the interfacial voids; the small voids would disappear and the larger voids would grow [27]. The schematic image of Cu joints after void ripening effect is presented in Fig. 13(d). In addition, the grain growth would happen at the stage of creep or void ripening. In Fig. 13, the abnormal grain growth happened at the creep stage. As increasing the annealing time, the joints of interfacial elimination would happen. The diffusion pathway transferred from grain boundary to lattice. The lattice diffusion coefficient was too low, so the interfacial voids would freeze in the final stage.

#### 4. Conclusions

In this study, TEM and FIB specimens were prepared to observe the plan-view images of void distribution in the Cu-to-Cu bonding interface. The evolution and ripening effect of the interfacial voids was analyzed at 250 °C for 5, 15, 30 and 120 min. However, a unique finding occurred at the 250 °C/120-min sample, where the interface was eliminated due to grain growth across the bonding interface, so the interfacial voids were embedded into a grain. This unique phenomenon also occurs in samples

#### Acknowledgements

The authors would like to acknowledge the funding support by the “Center for the Semiconductor Technology Research” from The Featured Areas Research Center Program within the framework of the Higher Education Sprout Project by the Ministry of Education (MOE), Taiwan; the Ministry of Science and Technology, Taiwan under Grant MOST 111-2634-F-A49-008 and Semiconductor Research Corporation (SRC), USA.

#### References

- [1] M.A. Dudek, L. Hunter, S. Kranz, J.J. Williams, S.H. Lau, N. Chawla, Three-dimensional (3D) visualization of reflow porosity and modeling of deformation in Pb-free solder joints, *Mater. Charact.* 61 (2010) 433–439, <https://doi.org/10.1016/j.matchar.2010.01.011>.
- [2] K. Oi, S. Otake, N. Shimizu, S. Watanabe, Y. Kunimoto, T. Kurihara, T. Koyama, M. Tanaka, L. Aryasomayajula, Z. Kutlu, Development of new 2.5D package with novel integrated organic interposer substrate with ultra-fine wiring and high density bumps, in: 2014 IEEE 64th Electron. Components Technol. Conf, 2014, pp. 348–353, <https://doi.org/10.1109/ECTC.2014.6897310>.

- [3] Y.C. Liang, C. Chen, K.N. Tu, Side wall wetting induced void formation due to small solder volume in microbumps of Ni/SnAg/Ni upon reflow, *ECS Solid State Lett.* 1 (2012) 60–62, <https://doi.org/10.1149/2.002204ssl>.
- [4] J. Utsumi, K. Ide, Y. Ichiyanagi, Cu/SiO<sub>2</sub> hybrid bonding obtained by surface-activated bonding method at room temperature using Si ultrathin films, *Micro Nano Eng.* 2 (2019) 1–6, <https://doi.org/10.1016/j.mne.2018.11.004>.
- [5] Y. Kagawa, N. Fujii, K. Aoyagi, Y. Kobayashi, S. Nishi, N. Todaka, S. Takeshita, J. Taura, H. Takahashi, Y. Nishimura, K. Tatani, M. Kawamura, H. Nakayama, T. Nagano, K. Ohno, H. Iwamoto, S. Kadomura, T. Hirayama, Novel stacked CMOS image sensor with advanced Cu<sub>2</sub>Cu hybrid bonding, in: 2016 IEEE Int. Electron Devices Meet 8, 2016, pp. 1–4, <https://doi.org/10.1109/IEDM.2016.7838375>.
- [6] Liang Wang, Gill Fountain, Bongsub Lee, Guilian Gao, Cyprian Uzoh, Scott McGrath, Paul Enquist, Sitaram Arkalgud, Laura Mirkarimi, Direct Bond Interconnect (DBI) for Fine-Pitch Bonding in 3D and 2.5D Integrated Circuits, 2017 Pan Pacific Microelectron. Symp. (Pan Pacific), 2017, pp. 1–6.
- [7] J.P. Mudrick, J.A. Sierra-Suarez, M.B. Jordan, T.A. Friedmann, R. Jarecki, M. D. Henry, Sub-10µm pitch hybrid direct bond interconnect development for die-to-die hybridization, *Electron. Components Technol. Conf.* (2019) 648–654, <https://doi.org/10.1109/ECTC.2019.00103>.
- [8] S.W. Kim, F. Fodor, N. Heylen, S. Iacovo, J. DeVos, A. Miller, G. Beyer, E. Beyne, Novel Cu/SiCN surface topography control for 1 µm pitch hybrid wafer-to-wafer bonding, *Electron. Components Technol. Conf.* (2020) 216–222, <https://doi.org/10.1109/ECTC32862.2020.00046>.
- [9] S.L. Chua, J.M. Chan, S.C.K. Goh, C.S. Tan, Cu-Cu bonding in ambient environment by Ar/N<sub>2</sub> plasma surface activation and its characterization, *IEEE Trans. Components Packag. Manuf. Technol.* 9 (2019) 596–605, <https://doi.org/10.1109/TCPMT.2018.2875460>.
- [10] T.H. Kim, M.M.R. Howlader, T. Itoh, T. Suga, Room temperature Cu–Cu direct bonding using surface activated bonding method, *J. Vac. Sci. Technol. A Vacuum Surf. Film.* 21 (2003) 449–453, <https://doi.org/10.1116/1.1537716>.
- [11] C.S. Tan, R. Reif, N.D. Theodore, S. Pozder, Observation of interfacial void formation in bonded copper layers, *Appl. Phys. Lett.* 87 (2005) 1–3, <https://doi.org/10.1063/1.2130534>.
- [12] J.Y. Juang, C.L. Lu, Y.J. Li, P.N. Hsu, N.T. Tsou, K.N. Tu, C. Chen, A solid state process to obtain high mechanical strength in Cu-to-Cu joints by surface creep on (111)-oriented nanotwins Cu, *J. Mater. Res. Technol.* 14 (2021) 719–730, <https://doi.org/10.1016/j.jmrt.2021.06.099>.
- [13] S.Y. Chang, Y.C. Chu, K.N. Tu, C. Chen, Effect of anisotropic grain growth on improving the bonding strength of <111>-oriented nanotwinned copper films, *Mater. Sci. Eng. A* 804 (2021) 1–9, <https://doi.org/10.1016/j.msea.2021.140754>.
- [14] J.J. Ong, W.L. Chiu, O.H. Lee, C.W. Chiang, H.H. Chang, C.H. Wang, K.C. Shie, S. C. Yang, D.P. Tran, K.N. Tu, C. Chen, Low-temperature Cu/SiO<sub>2</sub> hybrid bonding with low contact resistance using (111)-oriented Cu surfaces, *Materials* 15 (2022) 1888) 1–11, <https://doi.org/10.3390/ma15051888>.
- [15] J.Y. Juang, C.L. Lu, Y.J. Li, K.N. Tu, C. Chen, Correlation between the microstructures of bonding interfaces and the shear strength of Cu-to-Cu joints using (111)-oriented and nanotwinned Cu, *Materials* 11 (2368) (2018) 1–7, <https://doi.org/10.3390/ma11122368>.
- [16] C.M. Liu, H.W. Lin, Y.S. Huang, Y.C. Chu, C. Chen, D.R. Lyu, K.N. Chen, K.N. Tu, Low-temperature direct copper-to-copper bonding enabled by creep on (111) surfaces of nanotwinned Cu, *Sci. Rep.* 5 (2015) 1–11, <https://doi.org/10.1038/srep09734>.
- [17] J.Y. Juang, C.L. Lu, K.J. Chen, C.C.A. Chen, P.N. Hsu, C. Chen, K.N. Tu, Copper-to-copper direct bonding on highly (111)-oriented nanotwinned copper in no-vacuum ambient, *Sci. Rep.* 8 (2018) 1–11, <https://doi.org/10.1038/s41598-018-32280-x>.
- [18] K.C. Shie, A.M. Gusak, K.N. Tu, C. Chen, A kinetic model of copper-to-copper direct bonding under thermal compression, *J. Mater. Res. Technol.* 15 (2021) 2332–2344, <https://doi.org/10.1016/j.jmrt.2021.09.071>.
- [19] B. Rebhan, K. Hingerl, Physical mechanisms of copper-copper wafer bonding, *J. Appl. Phys.* 118 (2015), <https://doi.org/10.1063/1.4932146>, 135301–1–10.
- [20] Y.T. Wu, C. Chen, Low temperature Cu-to-Cu bonding in non-vacuum atmosphere with thin gold capping on highly (111) oriented nanotwinned copper, *J. Electron. Mater.* 49 (2020) 13–17, <https://doi.org/10.1007/s11664-019-07724-3>.
- [21] Y.P. Huang, Y.S. Chien, R.N. Tzeng, K.N. Chen, Demonstration and electrical performance of Cu-Cu bonding at 150 °C with Pd passivation, *IEEE Trans. Electron Devices.* 62 (2015) 2587–2592, <https://doi.org/10.1109/TED.2015.2446507>.
- [22] T.C. Chou, S.Y. Huang, P.J. Chen, H.W. Hu, D. Liu, C.W. Chang, T.H. Ni, C.J. Chen, Y.M. Lin, T.C. Chang, K.N. Chen, Electrical and reliability investigation of Cu-to-Cu bonding with silver passivation layer in 3-D integration, *IEEE Trans. Components Packag. Manuf. Technol.* 11 (2020) 36–42, <https://doi.org/10.1109/TCPMT.2020.3037365>.
- [23] S. Bonam, A.K. Panigrahi, C.H. Kumar, S.R.K. Vanjari, S.G. Singh, Interface and reliability analysis of Au-passivated Cu-Cu fine-pitch thermocompression bonding for 3-D IC applications, *IEEE Trans. Components Packag. Manuf. Technol.* 9 (2019) 1227–1234, <https://doi.org/10.1109/TCPMT.2019.2912891>.
- [24] Y.P. Huang, Y.S. Chien, R.N. Tzeng, M.S. Shy, T.H. Lin, K.H. Chen, C.T. Chiu, J. C. Chiou, C. TeChuang, W. Hwang, H.M. Tong, K.N. Chen, Novel Cu-to-Cu bonding with Ti passivation at 180 °C in 3-D integration, *IEEE Electron Device Lett.* 34 (2013) 1551–1553, <https://doi.org/10.1109/LED.2013.2285702>.
- [25] C.V. Thompson, R. Carel, Stress and grain growth in thin films, *J. Mech. Phys. Solids.* 44 (1996) 657–673, [https://doi.org/10.1016/0022-5096\(96\)00022-1](https://doi.org/10.1016/0022-5096(96)00022-1).
- [26] C.L. Lu, H.W. Lin, C.M. Liu, Y.S. Huang, T.L. Lu, T.C. Liu, H.Y. Hsiao, C. Chen, J. C. Kuo, K.N. Tu, Extremely anisotropic single-crystal growth in nanotwinned copper, *NPG Asia Mater.* 6 (2014) 1–8, <https://doi.org/10.1038/am.2014.90>.
- [27] H.C. Liu, A.M. Gusak, K.N. Tu, C. Chen, Interfacial void ripening in Cu-Cu joints, *Mater. Charact.* 181 (2021) 1–9, <https://doi.org/10.1016/j.matchar.2021.111459>.
- [28] Y. Jiang, R.C. Gu, M. Peterlechner, Y.W. Liu, J.T. Wang, G. Wilde, Impurity effect on recrystallization and grain growth in severe plastically deformed copper, *Mater. Sci. Eng. A* 824 (141786) (2021) 1–11, <https://doi.org/10.1016/j.msea.2021.141786>.
- [29] L. Vitos, A.V. Ruban, H.L. Skriver, J. Kollár, The surface energy of metals, *Surf. Sci.* 411 (1998) 186–202, [https://doi.org/10.1016/S0039-6028\(98\)00363-X](https://doi.org/10.1016/S0039-6028(98)00363-X).
- [30] A. Kuper, H. Letaw, L. Slifkin, E. Sonder, C.T. Tomizuka, Self-diffusion in copper, *Phys. Rev.* 96 (1954) 1224–1225, <https://doi.org/10.1103/PhysRev.96.1224>.